A comprehensive finite element framework for the progressive damage analysis of fiber metal laminate bolted joints under static and cyclic loading: theory and experimental validation

Christian Gerendt[a,*], Maryam Hematipour[a], Nils Englisch[b], Sven Scheffler[a], Raimund Rolfes[a]

[a] *Leibniz Universität Hannover, Institute of Structural Analysis, Appelstr. 9A, 30167 Hannover, Germany*
[b] *Fraunhofer IWES, Fraunhofer Institute for Wind Energy Systems, Fraunhofer Society, Am Seedeich 45, 27572 Bremerhaven, Germany*

Abstract

To improve the robustness of fiber-reinforced plastics (FRP) in bolted joints, local metal-hybridization of the FRP laminate can be performed to obtain an FRP-based fiber metal laminate (FML) of increased bearing strength. This contribution presents the first modeling framework able to predict the entire fatigue degradation process of such FRP-based FML bolted joints from damage initiation until ultimate failure, including the safety-relevant bolted joint failure mode. For this purpose, each laminate constituent material (i.e. metallic inlays and FRP plies) is analyzed by an own physically motivated continuum damage model. To predict the fatigue crack initiation and growth in the metallic inlays, the framework deploys a newly developed continuum damage approach, which uses a cyclic elasto-plastic strain energy increment as primary fatigue metric. Based on its constitutive equations, the inlay damage model is able to predict a fatigue crack's location and growth direction, both in the low- and the high-cycle fatigue regime. To account for the fatigue damage of the FRP plies, an energy-based fatigue damage approach for FRP composites, recently presented and validated by the authors, is applied. A comprehensive damage assessment is achieved as both fatigue models are accompanied by respective static damage models. The algorithms are implemented as one user-material (UMAT) subroutine in the commercial finite element software ABAQUS/Implicit. After the separate validation of the inlay damage model, the FML damage modeling framework is validated for open hole tension and T-bolt joint setups.

Keywords: Fiber metal laminates, Bolted joints, Fatigue damage, Finite element analysis, Experimental validation

*Corresponding authors
Email address: c.gerendt@isd.uni-hannover.de (Christian Gerendt)

1. Introduction

Fiber reinforced plastics (FRP) are used in numerous engineering applications such as energy, automotive or aviation, as they offer a high stiffness and strength, while being of comparatively low weight. However, FRP composites feature some fundamental shortcomings when applied in combination with bolted joints [1], which are a vital constructive detail for many engineering applications. By drilling the bolt hole, the load-carrying fibers of the FRP are severed, which in consequence initially lowers the load capacity of the joint. To compensate this "pre-damage" and to account for the complex stress states in the joint's periphery, quasi-isotropic laminates are usually applied near the bolts. This often requires a local thickening of the laminate, whereby the weight of the joint tends to increase and undesired load-eccentricities become more prominent [2]. In this context, the local metal-hybridization of the FRP laminate is a promising concept to create robust lightweight bolted joints in FRP composite structures. Starting from the so-called transition region, thin sheet metal inlays are utilized to systematically replace single plies of the FRP base-laminate [2], yielding an FRP-based fiber metal laminate (FML) in the bolt's periphery. With high-strength quasi-isotropic sheet metal inlays (e.g. stainless steel), even quite anisotropic laminates can withstand the complex stress states near the bolts without additional measures. The metallic inlays also support the ability of the laminate to plasticize without evolving critical damage, thereby increasing the overall amount of energy that is required to cause a final failure of the bolted joint. Metal-hybridization of FRP bolted joints thus effectively increases the bearing strength under quasi-static loading [3], and the fatigue resistance under cyclic loading [4].

However, to fully exploit the potential benefits of FML bolted joints, numerical models are required to predict and analyze the progressive damage processes both under quasi-static and cyclic loading. In [3], finite element analyses were performed to predict the progressive damage of FML bolted joints under quasi-static loading from damage initiation until ultimate failure. With the damage progress being correctly captured by the model for different failure modes of the joint, the predictive character and the physical integrity of continuum damage mechanics in combination with the finite element method (FEM) are demonstrated. To predict the fatigue behavior of FML bolted joints, fatigue initiation [5], fatigue damage [6] and post-fatigue residual strength [5] models were presented in the literature. These analytical fatigue models are developed for the analysis of FML with a high metal volume content (MVC $> 50\%$), and perform well for the respectively targeted joint failure mode, e.g. net-tension failure [6]. As for these models the primary constituent material of the FML is metal, and the failure mode of the joint is well defined, they do not need to account for fatigue damage of the FRP plies and also do not have to predict the resulting failure mode of the joint.

In contrast to that, this contribution focuses on the fatigue damage analysis of FRP-based FML bolted joints (featuring a minimal metal volume content), with the failure mode of the bolted joint being unknown in advance. For bolted joints, the failure mode is a highly valuable design aspect, as different failure modes feature different failure characteristics (sudden vs. progressive). As the FRP composite is the dominant constituent material of the herein considered FML, the fatigue degradation of the composite plies has a considerable influence on the overall fatigue behavior of the FML. Accordingly, the degradation of the FRP plies under cyclic loading must be captured by the model, to yield an accurate prediction of the FML degradation process. To be furthermore able to predict the bolted joint failure mode, the framework must closely capture the physics of (fatigue) damage for each of the constituent materials, i.e. metallic inlays and FRP plies. As the final joint failure mode is a natural outcome of the entire damage process, the model must be able to capture not only the state of damage propagation, but also the state of damage initiation. Last but not least, these abilities should be available in the low- and the high-cycle fatigue regime. This particularly demands the consideration of the elasto-plastic material behavior of the metallic inlays. Especially for the use-case of bolted joints, considerable plastic deformations of the metallic inlays are to observe already at moderate global load-levels.

In line with these thoughts, this contribution presents a novel finite element (FE) based modeling framework, which is able to predict the entire degradation process of FRP-based FML bolted joints under static and cyclic loading, starting from the first initiation of damage until ultimate failure. As the initiation and growth of damage in the metallic inlays and the FRP plies is governed by own physically motivated constitutive laws, the framework is able to forecast the failure mode of the joint in terms of a virtual test rig. The primary characteristics of the constituent materials' damage models are outlined in the following.

For the fatigue damage analysis of the metallic inlays, a novel continuum damage approach based on a cyclic elasto-plastic strain energy density increment [7] is presented, able to predict not only the inlay fatigue crack growth, but also its initiation. Due to the continuum damage representation of macroscopic fatigue cracks, the model is able to intrinsically account for arbitrary failure modes, i.e. crack locations and growth directions. Beside the pronounced predictive character of the model, the physical meaning of the applied energy increment also supports a straight forward experimental calibration of the model, as the the stress ratio effect (dependence of fatigue life on the applied stress ratio $R = \sigma_{min}/\sigma_{max}$ [8]) is efficiently suppressed. Accordingly, there is no demand for corrective algorithms like constant life diagrams, which are generally required to account for the stress ratio effect and need to be calibrated by a considerable amount of experimental data. As the fatigue metric explicitly takes into account the inlays' elasto-plastic material behavior, the model can be applied both in the low- and the high-cycle

fatigue regime. This is a strong advantage compared to linear-elastic fracture mechanics (LEFM), which is a widely established method to model the inlay fatigue crack growth in FML [6], but which is only valid when the global response of the material is elastic, i.e. in high-cycle fatigue regime. To account for static inlay rupture due to excessive (plastic) strains, the inlay fatigue damage model is furthermore accompanied by a strain-based static damage model [9]. The constitutive basis of the static-cyclic inlay damage model is provided by a nested-surfaces kinematic hardening plasticity model, originally presented in [10]. The plasticity algorithm is extended by the above damage algorithms to degrade the material's stiffness.

To account for intra-ply damage of the FRP layers both under static and cyclic loading, a static-cyclic FRP continuum damage model, recently presented and validated by the authors in [11], is applied. Here, the FRP fatigue damage is calculated based on an energy accumulation hypothesis [12], which includes the three-dimensional fracture criteria of Puck. By doing so, the physics of fatigue damage of the FRP composite are closely captured, while all dimensions of the stress space are taken into account. The three-dimensional fracture criteria of Puck are also used within the accompanying FRP static damage model.

The combination of both static-cyclic damage models, for the metallic inlays and the FRP plies, finally yields the novel static-cyclic FML damage model. The algorithms are implemented as a user-material (UMAT) subroutine in the commercial FE-software ABAQUS/Implicit.

To proof the validity of this novel FML damage model, experimental test on FML open hole tension (OHT) and FML T-bolt joint setups are conducted. Here, both quasi-static and cyclic loading conditions are considered. While the validation for the OHT specimens under cyclic loading is to demonstrate the validity of the framework for the low- and the high-cycle fatigue regime, the validation for the T-bolt joint demonstrates, that the framework is able to correctly predict the joint failure mode for complex setups. The accordance between experimental measurements and numerical results shows, that the presented framework fulfills the requirements defined within this section.

The paper is structured as follows: Section 2 explains the theoretical fundamentals of the novel inlay damage model, the coupling of the inlay and the FRP damage model, yielding the FML damage model, as well as general aspects concerning the analyzed FE-models. Section 3 introduces the experimental setups used for model calibration, verification and validation. In Section 4, the inlay damage model and finally the FML damage model are validated using first-hand experimental results. A conclusion of this study and an outlook to future follow-up research activities are given in Section 5.

2. Methodology

2.1. A continuum damage model for the metallic inlays of FML under quasi-static and cyclic loading

The constitutive basis for the static-cyclic inlay damage model is provided by a nested surfaces kinematic hardening plasticity model [10], which is implemented as an ABAQUS/Implicit user-material subroutine (UMAT). The plasticity model is able to account for nonlinear kinematic hardening and thus for a realistic simulation of the inlay's cyclic stress-strain behavior. In consequence, the calculation of the strain energy increment ΔW^{tot} becomes more accurate, which again is the primary fatigue metric used for the inlay material. The definition and utilization of ΔW^{tot} within the inlay fatigue damage model is explained later in this section. Concerning the plasticity algorithm, please refer to [10] for detailed information. In the following, the extension of the pristine plasticity algorithm by a static and a fatigue damage model is described.

First, the plasticity model from [10] is extended by a strain-based static damage model to account for inlay rupture in case of excessive plastic deformation. Based on the current plastic strain increment tensor $\Delta\boldsymbol{\varepsilon}^{pl}$, the equivalent plastic strain for the current increment $\varepsilon^{pl}_{eq,t_0+\Delta t}$ is determined. The equivalent plastic strain increment reads

$$\Delta\varepsilon^{pl}_{eq} = \frac{2}{3}\sqrt{\frac{3(\Delta {e^{pl}_{11}}^2 + \Delta {e^{pl}_{22}}^2 + \Delta {e^{pl}_{33}}^2)}{2} + \frac{3(4\Delta {\varepsilon^{pl}_{12}}^2 + 4\Delta {\varepsilon^{pl}_{23}}^2 + 4\Delta {\varepsilon^{pl}_{13}}^2)}{4}}, \tag{1}$$

with

$$\Delta e^{pl}_{11} = \frac{2}{3}\Delta\varepsilon^{pl}_{11} - \frac{1}{3}\Delta\varepsilon^{pl}_{22} - \frac{1}{3}\Delta\varepsilon^{pl}_{33}, \tag{2}$$

$$\Delta e^{pl}_{22} = -\frac{1}{3}\Delta\varepsilon^{pl}_{11} + \frac{2}{3}\Delta\varepsilon^{pl}_{22} - \frac{1}{3}\Delta\varepsilon^{pl}_{33}, \tag{3}$$

$$\Delta e^{pl}_{33} = -\frac{1}{3}\Delta\varepsilon^{pl}_{11} - \frac{1}{3}\Delta\varepsilon^{pl}_{22} + \frac{2}{3}\Delta\varepsilon^{pl}_{33}, \tag{4}$$

being the deviatoric components of the plastic strain increment tensor. The current equivalent plastic strain is defined to

$$\varepsilon^{pl}_{eq,t_0+\Delta t} = \varepsilon^{pl}_{eq,t_0} + \Delta\varepsilon^{pl}_{eq}. \tag{5}$$

With the equivalent plastic strain of the current increment at hand, the strain-based fracture criterion is evaluated. The so-called "fracture locus" defines the equivalent plastic strain at fracture initiation $\varepsilon^{pl}_{eq,ini}$

as a function of the stress-triaxiality η. The definition of the fracture locus as presented in [9] reads

$$\varepsilon^{pl}_{eq,ini} = \begin{cases} \infty & \text{for} \quad \eta \leq -1/3, \\ \dfrac{C_1}{1+3\eta} & \text{for} \quad -1/3 < \eta \leq 0, \\ C_1 + (C_2 - C_1) \cdot \left(\dfrac{\eta}{1/3}\right)^2 & \text{for} \quad 0 < \eta \leq 1/3, \\ C_2 \cdot \dfrac{1/3}{\eta} & \text{for} \quad 1/3 < \eta, \end{cases} \tag{6}$$

with $\eta = \sigma_{hyd}/\sigma_{vM}$, $C_2 = \varepsilon^{pl}_{eq,ini}(\eta = 1/3)$ (uniaxial tension) and $C_1 = \varepsilon^{pl}_{eq,ini}(\eta = 0) \approx 0.5 \cdot C_2$ (pure shear). Finally, the equivalent strain at ultimate failure $\varepsilon^{pl}_{eq,fail}$ is defined based on the fracture energy G_{fr} and the true uni-axial stress-strain curve, reading

$$\varepsilon^{pl}_{eq,fail} = \varepsilon^{tot}_{fail} = \frac{(G_{fr} - G_{hard}) \cdot 2}{l_c \cdot \sigma_{ini}} + \varepsilon^{tot}_{ini}, \tag{7}$$

with

$$\sigma_{ini} = \sigma(\varepsilon^{pl} = \varepsilon^{pl}_{eq,ini}), \tag{8}$$

$$\varepsilon^{tot}_{ini} = \varepsilon^{pl}_{eq,ini} + \frac{\sigma_{ini}}{E}, \tag{9}$$

and

$$G_{hard} = l_c \cdot \int_0^{\varepsilon^{tot}_{ini}} \sigma(\varepsilon^{tot})\, d\varepsilon^{tot}. \tag{10}$$

With the characteristic equivalent strains $\varepsilon^{pl}_{eq,t_0+\Delta t}$, $\varepsilon^{pl}_{eq,ini}$ and $\varepsilon^{pl}_{eq,fail}$ at hand, the static damage parameter for the inlay material is defined to

$$0 \leq D^{st}_{t_0+\Delta t} = \frac{u^{pl}_{eq,fail} \cdot (u^{pl}_{eq,t_0+\Delta t} - u^{pl}_{eq,ini})}{u^{pl}_{eq,t_0+\Delta t} \cdot (u^{pl}_{eq,fail} - u^{pl}_{eq,ini})} \leq 0.999 \quad \text{with} \quad u^{pl}_{eq} = \varepsilon^{pl}_{eq} \cdot l_c. \tag{11}$$

Defining the damage evolution in terms of equivalent plastic displacements u^{pl}_{eq}, thus incorporating the characteristic element length l_c, is to reduce the mesh-dependency in the softening regime. As suggested by Eq. 7, the model assumes no elastic strains at the state of complete damage, i.e. $D^{st} = 0.999$. For the sake of numerical stability, as well as thermodynamic consistency, it must be ensured that $D^{st}_{t_0+\Delta t} \geq D^{st}_{t_0}$, i.e. $\dot{D}^{st} \geq 0$. To further improve the numerical stability of the damage algorithm, the evolution of the damage variable is carefully damped, using the following equation:

$$D^{st,v}_{t_0+\Delta t} = \frac{\Delta t}{\eta^v + \Delta t} \cdot D^{st}_{t_0+\Delta t} + \frac{\eta^v}{\eta^v + \Delta t} \cdot D^{st,v}_{t_0}, \tag{12}$$

with $\eta^v \approx 0.001$ being a user-defined damping parameter [3] and Δt representing the (virtual) step time increment. The final stress state including the (damped) static damage parameter $D^{st,v}_{t_0+\Delta t}$ reads

$$\boldsymbol{\sigma}_{t_0+\Delta t} = (1 - D^{st,v}_{t_0+\Delta t}) \cdot \boldsymbol{C}_{\mathrm{UD}} \cdot (\boldsymbol{\varepsilon}^{el,trial}_{t_0+\Delta t} - \Delta\boldsymbol{\varepsilon}^{pl}). \tag{13}$$

Here, $\boldsymbol{\varepsilon}^{el,trial}_{t_0+\Delta t}$ represents the strain tensor of the elastic predictor step [10].
As a second extension of the original plasticity model, an energy-based fatigue damage model is developed to account for initiation and growth of macroscopic inlay fatigue cracks under cyclic loading. Inspired by the work of [7], the elasto-plastic strain energy density increment per cycle ΔW^{tot} (unit: $\mathrm{N/mm^2} = \mathrm{mJ/mm^3}$) is considered as the primary fatigue metric for the inlay material, reading

$$\Delta W^{tot} = \Delta W^{pl} + \Delta W^{e+}. \tag{14}$$

By taking into account the tensile elastic energy increment ΔW^{e+}, the model is able to account intrinsically for the mean stress effect [7]. The plastic energy increment ΔW^{pl} is of particular importance in the low-cycle fatigue regime, as pronounced plastic deformations dominate the fatigue process in such a case. Fig. 7 illustrates the two components of the energy increment ΔW^{tot} using in-situ experimental measurements. The tensile elastic energy increment is defined in the principal stress-strain space, reading

$$\Delta W^{e+} = \int_{H(\sigma_i^{min})\sigma_i^{min}}^{H(\sigma_i^{max})\sigma_i^{max}} = \frac{1}{2 \cdot (1 - D^{st,v}_{t_0+\Delta t})E} \left[(I_1^{max})^2 - \left(I_1^{min}\right)^2 \right] - \frac{1+\nu}{(1 - D^{st,v}_{t_0+\Delta t})E} \left[I_2^{max} - I_2^{min} \right], \tag{15}$$

with the two stress invariants being defined to

$$I_1^{max/min} = \sigma_1^{max/min} \cdot H(\sigma_1^{max/min}) + \sigma_2^{max/min} \cdot H(\sigma_2^{max/min}) + \sigma_3^{max/min} \cdot H(\sigma_3^{max/min}), \tag{16}$$

$$\begin{aligned} I_2^{max/min} = {} & \sigma_1^{max/min} \cdot H(\sigma_1^{max/min}) \cdot \sigma_2^{max/min} \cdot H(\sigma_2^{max/min}) \\ & + \sigma_2^{max/min} \cdot H(\sigma_2^{max/min}) \cdot \sigma_3^{max/min} \cdot H(\sigma_3^{max/min}) \\ & + \sigma_1^{max/min} \cdot H(\sigma_1^{max/min}) \cdot \sigma_3^{max/min} \cdot H(\sigma_3^{max/min}) \end{aligned} \quad . \tag{17}$$

Here, $H(...)$ represents a so-called Heaviside function, which is zero for negative (compressive) and one for positive (tensile) principal stress values [7]. The index max/min corresponds to a parameter's extreme values during a fully simulated load-cycle. The plastic energy increment is again defined in the regular stress-strain space, reading

$$\Delta W^{pl} = \Delta\sigma_{ij}\Delta\varepsilon_{ij} - 2\int_0^{\Delta\varepsilon_{ij}} \sigma_{ij}\, d\varepsilon_{ij} = \sum_{c=1}^{k} \frac{(\sigma_{ij,t_0} + \sigma_{ij,t_0+\Delta t}) \cdot (\varepsilon^{pl}_{ij,t_0+\Delta t} - \varepsilon^{pl}_{ij,t_0})}{2}, \tag{18}$$

with k being the total number of increments (index c) required for computing a full load cycle in the FEA, whereas σ_{ij} and $\varepsilon^{(pl)}_{ij}$ are the components of the three-dimensional stress and (plastic) strain tensor,

respectively. A parameter's range during the full load cycle is represented by Δ. After the simulation of a full load cycle and with the total energy increment ΔW^{tot} at hand, the actual inlay fatigue damage algorithm can be executed.

To detect whether of not the fatigue process has been initiated, the inlay fatigue damage model evaluates an experimentally determined ΔW^{tot}-N_F relation of the inlay material, illustrated in Fig. 1. As shown in Fig. 1, the energy increment is a quite efficient metric for the fatigue assessment of the metallic inlays, since it features an intrinsic validity for various mean stresses, i.e. stress-ratios. This intrinsic validity makes the approach highly applicable for use-cases featuring complex stress distributions, as for example bolted joints. Here, local stress concentrations are likely to occur near the bolts, including tensile and compressive stresses. In addition to that, the material characterization effort can be reduced significantly, as theoretically only one R-ratio needs to be experimentally examined. In contrast to that, traditional fatigue metrics, like stress or strain, exhibit a pronounced mean stress dependence, considerably exacerbating the experimental characterization process [8]. Based on the least-square method fit of the experimental ΔW^{tot}-N_F relation (compare Fig. 1), the number of cycles to crack initiation reads

$$N_F = \left(\frac{\Delta W^{tot} - C_{ini}}{\kappa_{ini}} \right)^{\frac{1}{\alpha_{ini}}} . \tag{19}$$

The parameters κ_{ini}, α_{ini} and C_{ini} for the monolithic inlay material (stainless steel EN 1.4310) are provided in Table 2. If the fatigue threshold is not exceeded, i.e. $\Delta W^{tot} \leq \Delta W^{tot}_{th} \approx 1$ N/mm^2, the fatigue analysis is skipped, assuming a domain of infinite fatigue life. However, the total energy accumulated cyclically, reading

$$W^{tot}_{new} = W^{tot}_{old} + \Delta n \cdot \Delta W^{tot}, \tag{20}$$

is updated even if $\Delta W^{tot} \leq \Delta W^{tot}_{th}$ to provide continuous energetic consistency of the fatigue algorithm, just in case the fatigue initiation criterion is met at a later point in time. In case $\Delta W^{tot} > \Delta W^{tot}_{th}$, the updating procedure of the inlay fatigue damage parameter is performed. First, the already accumulated energy W^{tot}_{old} needs to be converted into an equivalent number of applied cycles n_{eq} with respect to the current energy increment value ΔW^{tot}, reading

$$n_{eq} = \frac{W^{tot}_{old}}{\Delta W^{tot}}. \tag{21}$$

This step is of considerable importance to ensure energetic consistency of the algorithm. Accordingly, the total number of cycles theoretically applied for current "load-level" ΔW^{tot} sums up to $n = \Delta n + n_{eq}$, with Δn representing the actual virtual repetitions of the current load-cycle in terms of a cycle-jump

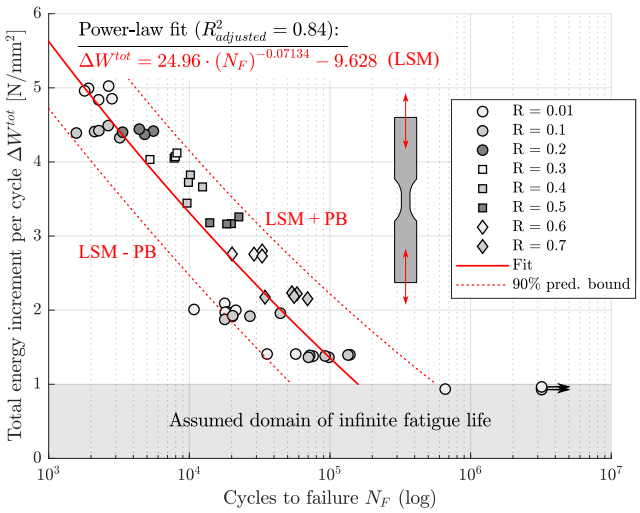

Figure 1: ΔW^{tot}-N_F relation experimentally determined for the FML stainless steel inlay material. "Runouts" are marked with black arrows, yielding the endurance limit $\Delta W^{tot}_{th} \approx 1 N/mm^2$. Abbreviations used: LSM - least square method fit, PB - prediction bound. Further details on the underlying experimental procedure are given in Section 3.

technique. To check if fatigue damage is evolving, the normalized lifetime is evaluated, reading

$$\frac{n}{N_F(\Delta W^{tot})} \begin{cases} \geq 1 & \rightarrow \quad D^{fat}_{new} = D^{fat/st}_{old} + \Delta n \cdot \dot{D}^{fat} = D^{fat/st}_{old} + \Delta n \cdot \dfrac{C_{cg} E^{m_{cg}/2} \left(\Delta W^{tot} \cdot l_c\right)^{m_{cg}/2}}{l_c} \\ < 1 & \rightarrow \quad D^{fat}_{new} = D^{st}_{old} \quad \text{and} \quad W^{tot}_{new} \text{ acc. to Eq. 20} \end{cases} , \tag{22}$$

with $\dot{D}^{fat} \geq 0$ being the rate of fatigue damage per cycle [13]. In case the lifetime has been exceeded, i.e. $n/N_F(\Delta W^{tot}) \geq 1.0$, fatigue crack growth is considered to start. Here, the material constants C_{cg} and m_{cg} in Eq. 22 are parameters defining the steady crack growth behavior of the inlay material. According to [14], the parameters C_{cg} and m_{cg} can be chosen in close accordance with the parameters defining the material's Paris crack growth curve. The characteristic element length l_c is again introduced to reduce the mesh-dependency of the algorithm during softening, and also to convert the crack growth rate into a non-dimensional continuum damage parameter. It should be noted, that the old damage in Eq. 22 can also be represented by previous static damage (st), creating a consistent link between static and fatigue damage. The final stress state is again determined according to Eq. 13, whereby the larger damage parameter (D^{st} vs. D^{fat}) is decisive and viscous damping according to Eq. 12 is constantly applied. Finally, a strain perturbation scheme is applied to numerically approximate the Jacobian matrix $\partial \Delta\sigma / \partial \Delta\varepsilon$, which is demanded by the implicit solver after each call of the subroutine to perform the iterative Newton-

Raphson scheme [15].

2.2. A comprehensive progressive damage model for FML under quasi-static and cyclic loading

The comprehensive FML damage model is created by combining the above static-cyclic inlay damage model with a static-cyclic progressive intra-ply FRP damage model recently presented by the authors in [11] . To calculate the fatigue damage of an unidirectional (UD) FRP ply, the model from [11] adapts an energy hypothesis originally developed for the fatigue analysis of reinforced concrete, see [12]. To quantify fatigue damage in terms of stiffness degradation, the hypothesis states that the material degradation under quasi-static loading is comparable to the degradation under cyclic loading, given that the same amount of mechanical energy has been accumulated by a material point. From a theoretical viewpoint, this allows to quantify the fatigue damage D^{fat}, corresponding to a given amount of accumulated fatigue energy g^{fat}, basically by integrating the quasi-static stress-strain relation of the UD FRP composite, yielding $g^{st}(D^{st})$, until $g^{st} \approx g^{fat}$. According to the theory from [12], in this case the static damage D^{st} corresponds to the fatigue damage D^{fat}. It is to note, that the algorithm is performed for each of the principle directions of the UD ply, i.e. fiber direction, transverse direction and shear, yielding the damage fatigue parameters D_F^{fat}, D_M^{fat} and D_S^{fat}. The damaged material stiffness for a particular principle direction of the UD ply then generally reads

$$E_D = E \cdot \left(1 - D^{fat/st}\right). \tag{23}$$

By coupling this FRP fatigue algorithm with a static FRP damage model based on the fracture criteria of Puck [16], a comprehensive FRP damage model is created, able to account for static and fatigue damage alike. For further insights concerning the FRP (fatigue) damage algorithm please refer to [11]. Due to the successful validation of the static-cyclic FRP damage model for FRP bolted joints in [11], a separate validation of the FRP damage model is skipped in the current study. Both static-cyclic damage models (inlay and FRP) are finally implemented as one ABAQUS/Implicit user-material subroutine (UMAT). As for all UMAT implementations, every operation will be performed on Gauss point level. To distinguish between the two different materials in a laminate, namely FRP and metal, the material definition of a Gauss point is checked at the beginning of each subroutine call. Depending on the present material declaration, defined during build-up of the FE-model, either the FRP damage model (see [11]) or the inlay damage model from Section 2.1 is executed. Fig. 2 presents an illustrative display of the FML damage model workflow.

The fulfillment of the global mechanical equilibrium, continuously demanded by the implicit solver (ABAQUS/Implicit), results in a consistent interaction of the damage models. Due to the layer-wise analysis scheme, no laminate-related information is required for the analyses, despite the stacking sequence.

With access to the various modeling techniques available in the commercial FE-software ABAQUS/CAE, the presented FML damage model becomes a comfortably to apply tool for progressive damage analyses of FML in complex use-cases like bolted joints under quasi-static and cyclic loading conditions.

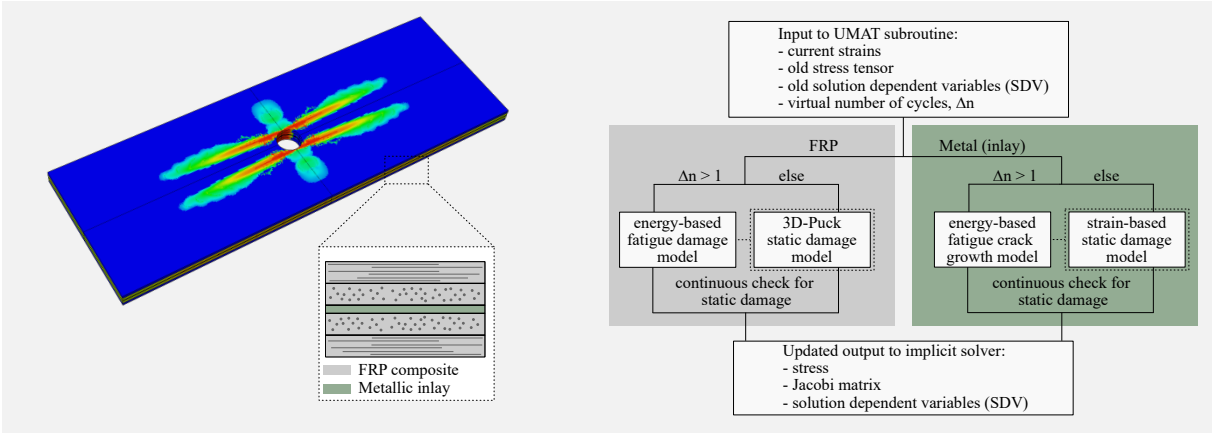

Figure 2: Schematic illustration of the FML damage model work-flow. The material damage algorithms are implemented in one user-material subroutine for ABAQUS/Implicit (UMAT). Typical solution dependent variables (SDV) are for example plastic strains or damage parameters.

2.3. General modeling aspects

In this section, general aspects concerning the analyzed FE-models are outlined. In all models, fully-integrated volume elements (type C3D8 in ABAQUS/Implicit) are applied. To increase the efficiency of the performed analyses, only quarters of the test setups are modeled. Among the analyzed models of this study, the FML T-bolt joint setup is the most complex. T-bolt joints are generally used to connect the rotor blades of wind turbines to the turbine's hub [17]. Here, these joints are primarily exposed to fatigue loading (regular operating conditions), but also need to withstand extreme loads like gusts or emergency stops. During experimental testing, the T-bolt specimen is firmly applied to the steel counterbearing by torquing the nut of the horizontal bolt, compare Fig. 3. Referring to the use-case of a wind turbine blade, the counterbearing represents the hub of the turbine's rotor. Torquing is stopped after reaching a tensile pre-strain of about 2000 μm/mm within the horizontal bolt. After that, the setup is ready to be tested. In the FEA, the horizontal bolt is modeled as a linear-elastic rod, neglecting the nut, the washer and other insignificant details. The elastic stiffness of the horizontal bolt is defined to $E = 210$ GPa, with a standard Poisson's ratio of $\nu = 0.3$. In line with the aforementioned experimental procedure, the free-end of the elastic horizontal bolt is deflected until the targeted tensile pre-strain of ca. 2000 μm/mm is reached all throughout the horizontal bolt. The elastic horizontal bolt

is again attached to the vertical bolt by using a kinematic constraint. As the vertical bolt and also the counterbearing of the T-bolt setup are much stiffer than the FML specimens, both parts are modeled to be perfectly rigid, thus saving again computational resources. Furthermore, in-house contact definitions available in ABAQUS/CAE are applied at the respective interfaces between the bolt, the counterbearing and the laminate. Here, a friction coefficient of $\mu = 0.3$ is used. The primary loading is applied via a single reference point, which is coupled to the specimens free end using again a kinematic constraint, compare Fig. 3. The symmetric laminate stacking for the FML T-bolt specimens reads from top to

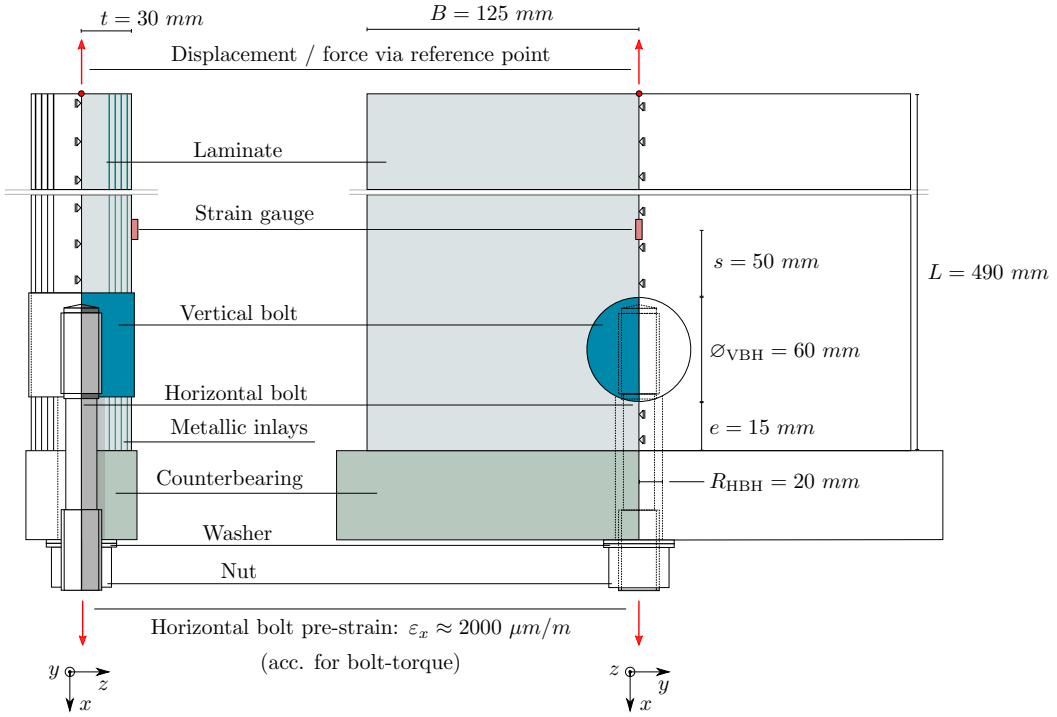

Figure 3: Schematic illustration of the FML T-bolt bearing test setup. The areas which are part of the finite element quarter-model are colored. Via the laminate reference point (red dot) a pulsating force is applied during fatigue analyses, whereas in the quasi-static analyses the reference point is continuously deflected, compare also Section 3.

centerline $[\mathrm{Tx}\ ;\ ((\mathrm{Bx}\ ;\ \mathrm{SS}\ ;\ \mathrm{Bx})\ ;\ \mathrm{Tx}_2)_4\ ;\ (\mathrm{Bx}\ ;\ \mathrm{Tx}_2)_6\ ;\ \mathrm{Tx}_4]_S$, with "Tx" representing a $[0°\ ;\ \pm 45°]$ triaxial non-crimped fabric, "Bx" representing a $[\pm 45°]$ biaxial non-crimped fabric and "SS" representing the stainless steel inlays of 0.25 mm thickness, grade EN 1.4310. To model the GFRP composite non-crimped fabric (NCF) plies as a layup of differently orientated unidirectional (UD) plies (as required by the FRP damage model), a transfer scheme based on the NCF fiber grammage and a UD base-laminate is applied. To apply this NCF modeling scheme, it is required that the resin and fibers of the NCF and the UD base-laminate share similar stiffness and strength properties. For further details concerning the

NCF modeling technique please refer to [11]. The nominal thicknesses of the two NCF after curing, the total fiber grammage, the grammage per fiber orientation and finally the modeled ply thickness of the UD base-laminate per orientation are listed in the following:

- Triax: $t_{triax} = 0.83$ mm with 1211 g/m^2 NCF $\begin{cases} 0^\circ & : \quad 709 \text{ g/m}^2 \rightarrow 58\% \approx 0.48 \text{ mm} \\ +45^\circ & : \quad 251\ g/m^2 \rightarrow 21\% \approx 0.17 \text{ mm} \\ -45^\circ & : \quad 251\ g/m^2 \rightarrow 21\% \approx 0.17 \text{ mm} \end{cases}$
- Biax: $t_{biax} = 0.56$ mm with 1202 g/m^2 NCF $\begin{cases} +45^\circ & : \quad 601 \text{ g/m}^2 \rightarrow 50\% = 0.28 \text{ mm} \\ -45^\circ & : \quad 601 \text{ g/m}^2 \rightarrow 50\% = 0.28 \text{ mm} \end{cases}$

The layup of FML open hole tension (OHT) specimens reads [0° ; 90° ; SS ; 90° ; 0°], with the FRP plies being of about 0.85 mm thickness each. The geometrical properties of the stainless steel sheet metal and the FML OHT specimens are given in Fig. 4. As for the T-bolt joint setup, all symmetry

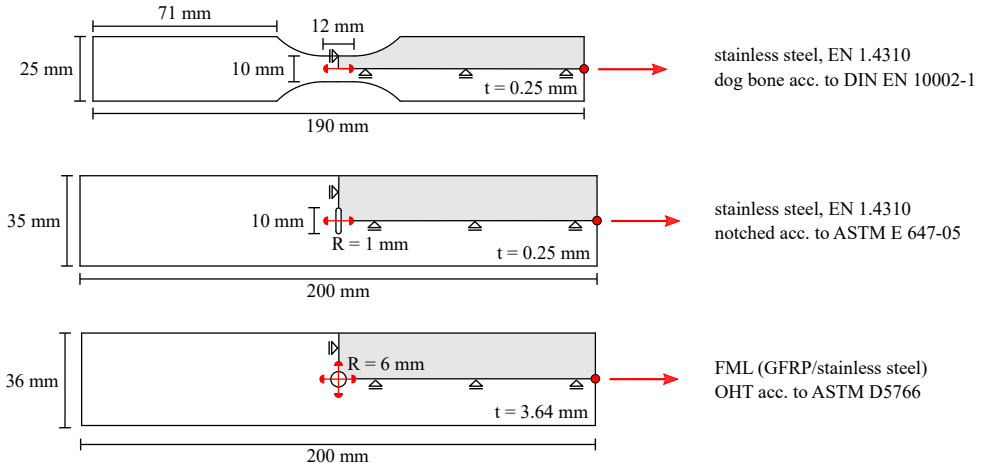

Figure 4: Stainless steel sheet metal and FML open hole tension (OHT) specimens used for calibration, verification and validation of the FML damage model. The positions of the virtual DIC extensometers are marked in red. The respective specimen thickness is represented by "t", radii are represented by "R". Via the laminate reference point (red dot) a pulsating force is applied during fatigue analyses, whereas in the quasi-static analyses the reference point is continuously deflected, compare also Section 3. The areas which are part of the finite element quarter-model are colored.

planes are considered to gain a maximal computational efficiency of the model. Thus, only a quarter of the actual setup is taken into account by the respective FE-models. The properties of the UD base material, used as input for the FRP damage model, are given in Tab. 1. The material properties used as input for the inlay damage model are listed in Table 2. The fatigue analyses are performed using multiple ABAQUS/Implicit static general steps. Each step represents a full load cycle (from maximum

E_{11} [GPa]	E_{22} [GPa]	E_{12} [GPa]	ν_{12}	ν_{23}
42	12	3.44	0.28	0.38
$R_{11,T}$ [MPa]	$R_{22,T}$ [MPa]	$R_{11,C}$ [MPa]	$R_{22,C}$ [MPa]	R_{12} [MPa]
1005	48	813	152	57
$G_{11,T}$ [N/mm]	$G_{22,T}$ [N/mm]	$G_{11,C}$ [N/mm]	$G_{22,C}$ [N/mm]	G_{12} [N/mm]
64	1.8	80	16	2.7

Table 1: Static material properties of the GFRP used as input for the FRP damage model. The values represent the mean values out of multiple valid static characterization tests according to ASTM standards. The fracture energies G were determined as explained in [3]. For the sake of brevity, please refer to [11] concerning the GFRP's fatigue material parameters.

E [GPa]	ν	$\varepsilon^{pl}_{eq,ini}(\eta = 1/3)$	G_{fr} [N/mm]	m_{cg}	K_{RO} [MPa]
175	0.3	0.45	200	2.2	1281
C_{cg} [MPa$^{-m_{cg}}$mm$^{1-m_{cg}/2}$]	κ_{ini}	α_{ini}	C_{ini} [MPa]	ΔW^{tot}_{th} [MPa]	n_{RO}
$3.097 \cdot 10^{-11}$	24.96	-0.0713	-9.628	1	0.0718

Table 2: Basic material properties used as input for the inlay damage model. The parameters m_{cg} and C_{cg} to define the fatigue damage evolution are taken from [18]. All other parameters were obtained experimentally in this study. For further information on how to configure the plasticity model for a given uniaxial stress-strain curve please refer to [10]. K_{RO} and n_{RO} represent the Ramberg-Osgood parameters to define the cyclic stress-strain curve.

to minimum and back to maximum loading), being associated with Δn virtual repetitions, which are used in terms of a cycle jump scheme (compare for example Eq. 22). As static general analysis steps naturally ignore any dynamic effects, the inertia of the specimens is omitted.

3. Experimental setups

3.1. Experimental characterization of the FML metallic inlay material

The testing of the stainless steel sheet metal (grade EN 1.4310) used as metallic inlays of the herein considered FML has been conducted with a 100 kN servo-hydraulic testing machine. A 12.5 kN load-cell has been installed for force measurement and control. The two different sheet metal specimens displayed in Fig. 4 were cut by a water-jet. Afterwards, the (outer) edges of the specimens were sanded carefully until a sufficient edge quality was achieved. To prevent premature damaging of the specimens during clamping, end-tabs made from $\pm 45^\circ$ GFRP were glued on both ends and sides of the specimens. The end-tabs were chamfered by sanding prior to application to yield a sufficiently smooth load introduction into the actual

specimen. To measure the deformations of the specimens during testing, a digital image correlation (DIC) device has been integrated into the test setup, see Fig. 5. To prepare for DIC measurements, the specimens were degreased, coated with white primer and subsequently sprackled with black paint to obtain a stochastic black and white pattern. To determine the ΔW^{tot}-N_F relation of the inlay material

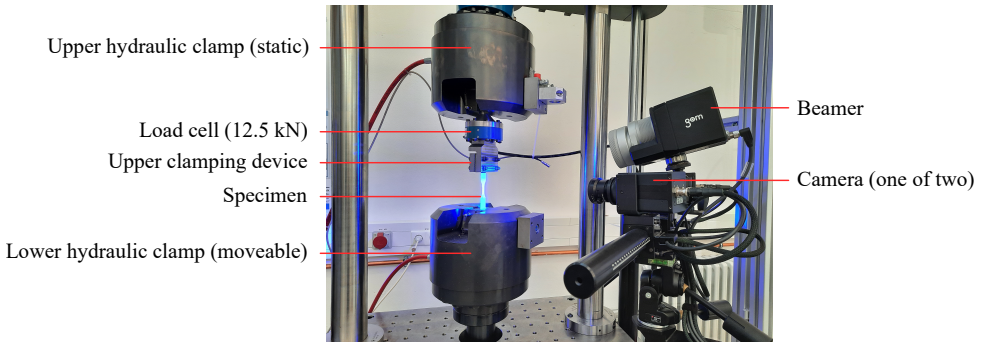

Figure 5: Photo of the setup used for testing of the stainless steel sheet metal and the FML open hole tension specimens.

(see Fig. 1), fatigue tests were performed using the dog bone specimens displayed in Fig. 4. The dog bone fatigue tests were sectioned into three phases, with the ΔW^{tot}-recording being performed in the second phase only, see Fig. 6. By converting the engineering strain of the DIC extensometer into true strain, and the force signal of the test machine into true stress, an in-situ measurement of the strain energy density increment per cycle ΔW^{tot} was achieved. Per definition, the plastic energy increment ΔW^{pl} corresponds to the area enclosed by the stress-strain hysteresis (Eq. 18), whereas ΔW^{e+} corresponds to the area below the hysteresis (Eq. 15), compare Fig. 7. To measure the energy increment per cycle ΔW^{tot} with a minimal influence of the natural white noise of the DIC device, as well as material damping effects, the test frequency was set to 0.01 Hz during the hysteresis recording phase, while the DIC recording frequency was kept constantly at 200 Hz (yielding 20.000 data points per cycle). The true stress and strain data for one load cycle was then used to fit two sine functions, one for strain and one for stress. Afterwards, both sine fits were combined to create a fit of the true stress-strain hysteresis, which finally could be examined numerically to determine the in-situ energy increment ΔW_i^{tot} for one cycle i of the hysteresis recording phase. The fitting procedure has been performed for each of the $1 \leq i \leq 100$ cycles of the recording phase. The value of ΔW^{tot}, used to define one of the experimental ΔW^{tot}-N_F data points in Fig. 1, is the mean value of these 100 single ΔW_i^{tot} values. After the recording phase the tests were continued with an increased test frequency ($5 - 15$ Hz) to finally cause fatigue failure in an appropriate time span, yielding the value of N_F. This scheme has been repeated for different load-levels and stress ratios, whereas only constant amplitude loading was applied. It is also to note, that only

swelling tension test could be performed, as the sheet metal, with a thickness of just 0.25 mm, would have buckled under the slightest compression. Using an anti-buckling device was also inappropriate, as the recording via DIC would have been impossible. The usage of a mechanical extensometer being attached laterally to the specimens was also to discard, as the small available contact interface comprises the hazard of extensometer slippage. Anyhow, to allow for a proper calibration of the inlay plasticity model, the quasi-static and the cyclic stress-strain curve were also determined experimentally. To determine the static stress-strain curve, displacement-driven tests were conducted, featuring a displacement rate of 0.01 mm/sec. To determine the cyclic stress-strain curve, the maximum stress $\sigma_{max,i}$ and strain $\varepsilon_{max,i}$ values for each of the 100 hystereses in the hysteresis recording phase were recorded. By computing the respective means from these two data sets, one experimental data point of the cyclic stress-strain relation is obtained.

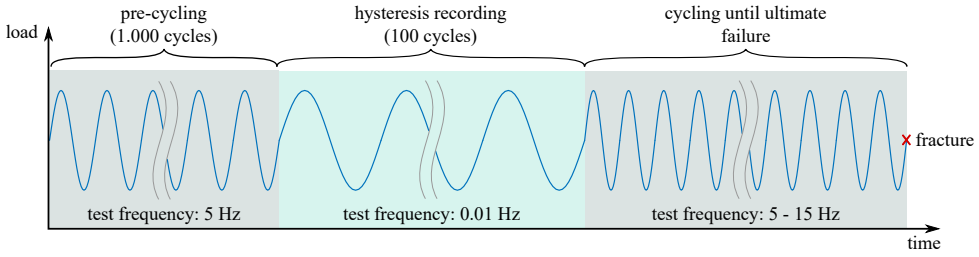

Figure 6: Different phases of a fatigue test conducted for the dog bone stainless steel specimens. The test frequency in the third phase was chosen with respect to the expected lifetime (the longer the expected lifetime, the higher the test frequency). The DIC system was set for a constant recording frequency of 200 Hz.

The centered notched stainless steel specimens were tested for a separated validation of the inlay damage model. Here, a virtual extensometer crossing the notch in load direction was used as primary deformation and damage metric, respectively, see Fig. 4. The quasi-static tests were performed with a displacement rate of 0.01 mm/sec, whereas a constant test frequency of 5 Hz and a force-ratio of $R = F_{min}/F_{max} = 0.1$ (constant amplitude, global tension-tension) were applied for cyclic testing. The recording frequency of the DIC device was set to 100 Hz.

3.2. FML open hole tensile tests under quasi-static and cyclic loading

Using almost the same test setup introduced previously in Section 3.1 (despite switching to a 100 kN load-cell), FML open hole tension (OHT) specimens were tested under quasi-static and cyclic loading to provide the experimental data for a first validation of the FML damage model. The specimens were manufactured by vacuum assisted resin infusion (VARI) and cut by a water-jet. Thus, no additional adhesive has been applied to bond the FRP plies and the metallic inlays. The stainless steel inlays were

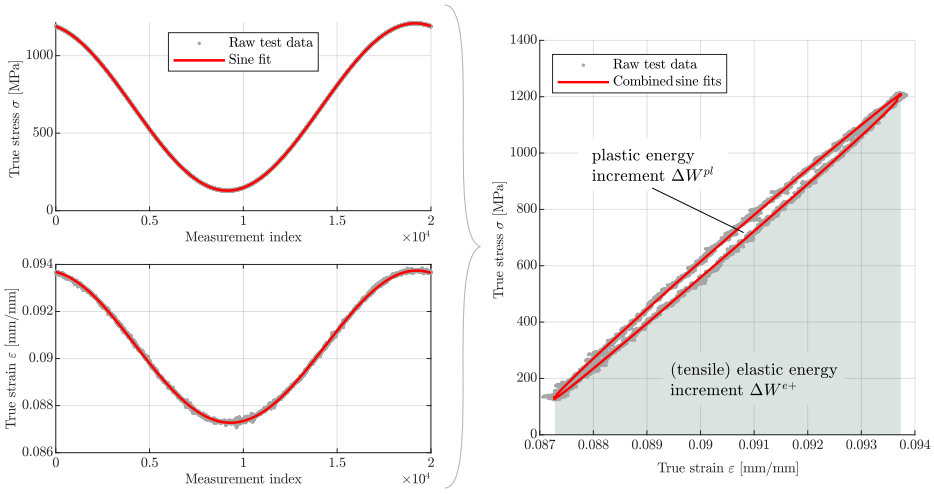

Figure 7: Illustration of the post-processing of the true stress and strain data obtained for the stainless steel dog bone specimens during the "hysteresis recording phase" (second phase Fig. 6). The strain energy density increment per cycle reads $\Delta W^{tot} = \Delta W^{pl} + \Delta W^{e+}$. The procedure is repeated for each of the 100 recorded hystereses.

pre-treated, both mechanically (sandblasted) and chemically (Sol-gel coating), to provide an optimal adhesive bond with the GFRP plies. The static tests were again conducted displacement-driven, applying a deflection rate of 0.01 mm/sec. The fatigue tests were conducted force-driven, with a target force-ratio of $R = F_{min}/F_{max} = 0.1$ (constant amplitude, global tension-tension) and a test frequency of 5 Hz. The recording frequency of the DIC device was set to 5 and 100 Hz for static and fatigue loading, respectively. For both load cases, the deformation of the central hole has been used to quantify the extend of damage of the specimen. More in particular, the central hole has been measured continuously using two DIC virtual extensometers, crossing the hole vertically and horizontally, compare Fig. 4.

3.3. FML T-bolt joints under quasi-static and cyclic loading

The FML T-bolt bearing tests were conducted to validate the FML damage model for a complex bolted joint use-case on sub-component level. As these joints feature a quite complex damage behavior, they represent an excellent application to demonstrate the abilities of the presented FML damage model. To increase the general load capacity of the FML T-bolt joint compared to a pure GFRP design (compare [11]), eight stainless steel inlays (grade EN 1.4310) of 0.25 mm thickness each were integrated into the GFRP base-laminate. As displayed in Fig. 3, the steel inlays were placed at the outer regions of the stacking to strengthen the weakest part of the laminate, while at the same time ensuring a "GFRP-only" drilling for the horizontal bolt hole. The steel sheets were again pre-treated both mechanically (sand-blasted) and chemically (Sol-gel coating) for an optimal bonding with the GFRP plies. The specimens

were manufactured using the VARI technique. For performing the tests, a 2500 kN servo-hydraulic test machine was used, able to deal with the high forces expected for these massive specimens. The static tests were conducted displacement-driven, whereas the fatigue tests were conducted force-driven, with a target force-ratio of $R = F_{min}/F_{max} = 0.1$ (constant amplitude, global tension-tension).

4. Results and discussion

4.1. Validation of the inlay damage model

To validate the static module of the static-cyclic inlay damage model, the results of the static tension tests conducted for the centered notched stainless steel sheet metal specimens are examined. To quantitatively compare the accordance of the numerical simulation and the experimental measurements, the machinery reaction force is plotted as a function of the percentage notch elongation in load-direction, see Fig. 8. The material model is able to capture the mechanical response of the notched specimens in the pre-damage state and the steady rupture in the softening state in proper accordance with the experimental measurements.

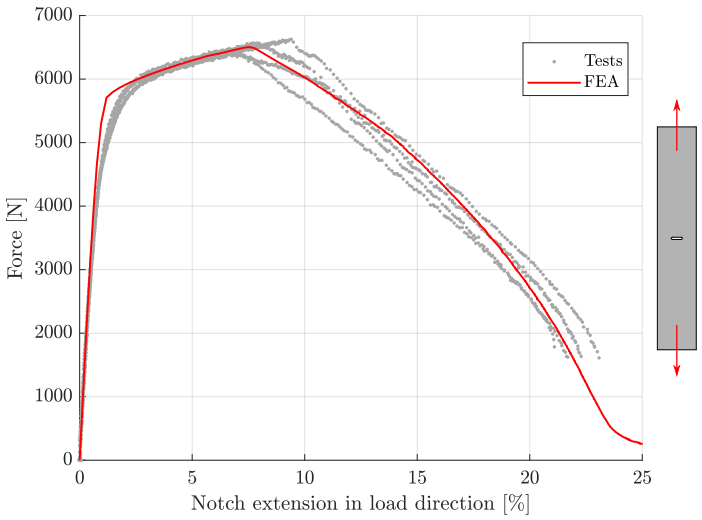

Figure 8: Validation of the FML inlay static damage model using the test results obtained for the centered notched stainless steel specimens under quasi-static tensile loading.

Next, the validity of the fatigue module of the static-cyclic inlay damage model is examined using the results of the cyclic tests conducted for the centered notched stainless steel specimens. As for the static campaign, the percentage notch elongation in load-direction is used for comparison of the numerical predictions and the experimental measurements. Fig. 9 illustrates that the model is generally able to predict

the onset and progress of the fatigue crack growth in accordance with the experimental measurements. Though, the number of cycles until crack initiation for the intermediate load-level (0.40 x UTS) is slightly overestimated. The cause for the overestimation has not been finally clarified yet. It is to assume that the offset can be traced back to the fatigue damage initiation criterion, as the damage rate in terms of percentage notch extension increase is nevertheless in close accordance with the experimental results ($0.4 \rightarrow 0.8\%$ within about $1.3 \cdot 10^4$ cycles). However, the inlay damage model is furthermore proven to be sufficiently robust, as the model is able to fully capture the rapid notch extension increase right before ultimate fatigue failure.

The overall quality of the obtained results for the separate validation of the static-cyclic inlay damage model is considered to allow to further proceed with the validation of the static-cyclic FML damage model in the next section.

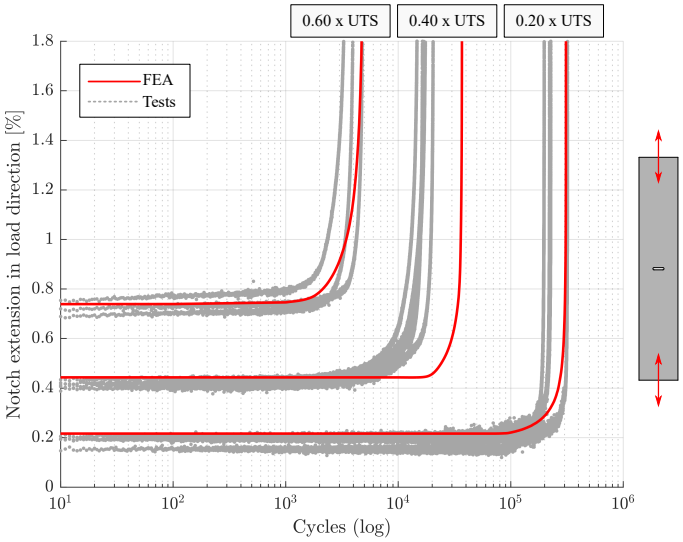

Figure 9: Comparison of the fatigue tests results obtained for the centered notched stainless steel specimens and respective predictions of the inlay damage model. Three different load-levels (represented by percentages of the ultimate tensile strength, UTS) were examined, applying a constant amplitude loading with a stress-ratio $R = 0.1$ (global swelling tension).

4.2. Validation of the FML damage model

To validate the static-cyclic FML damage model on coupon-level, the experimental results of the FML open hole tension (OHT) tests for quasi-static and cyclic loading are considered. The results of the quasi-static tensile tests in comparison with the respective numerical prediction are displayed in Fig. 10. The comparison in Fig. 10 shows that the model captures the initial stiffness of the specimen, the maximum force, i.e. specimen strength, as well as the post-strength softening in close accordance

with the experimental measurements. However, since the FRP material model does not account for shear-nonlinearity, the model slightly overestimates the initiation of shear-damage near the hole and, in consequence, the hole elongation in load direction. Despite this acceptable offset, the overall mechanics of the OHT specimen are captured sufficiently accurate to continue with the fatigue analyses of the setup. Fig. 11 shows the experimentally measured hole elongation in load-direction over the applied number

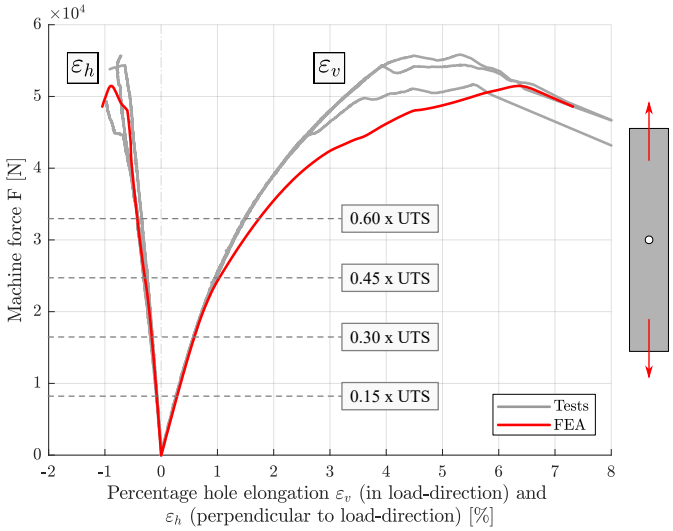

Figure 10: Simulation of the quasi-static FML open hole tension setup in comparison with experimental measurements of the percentage hole elongation in load-direction and perpendicular to the load-direction. The four labels represent the maximum load-levels applied for the following fatigue campaign.

of cycles for different load-levels (percentage of the ultimate tensile strength, UTS) in comparison with the respective numerical predictions. The close agreement between simulation and experiment for the different load-levels demonstrates the applicability and validity of the FML damage model both for the low- and the high-cycle fatigue regime. Especially for the low-cycle fatigue regime the consideration of inlay-plasticity (compare Eq. 14) is highly relevant, as the inlay exhibits considerable plastic deformation directly after the maximum fatigue load is applied.

To further demonstrate the abilities of the model for a more complex use-case, the quasi-static and cyclic FML T-bolt joint setups are simulated and compared to respective experimental results in the following. First, a quasi-static loading-unloading scenario is simulated to verify the FE-model of the T-bolt setup. The results shown in Fig. 12 illustrate that the experimentally measured force-strain relation is predicted quite accurately by the FML damage model. The intermediate offset between simulation and experiment at the end of the unloading-path is assumed to be caused by inlay-buckling in the area

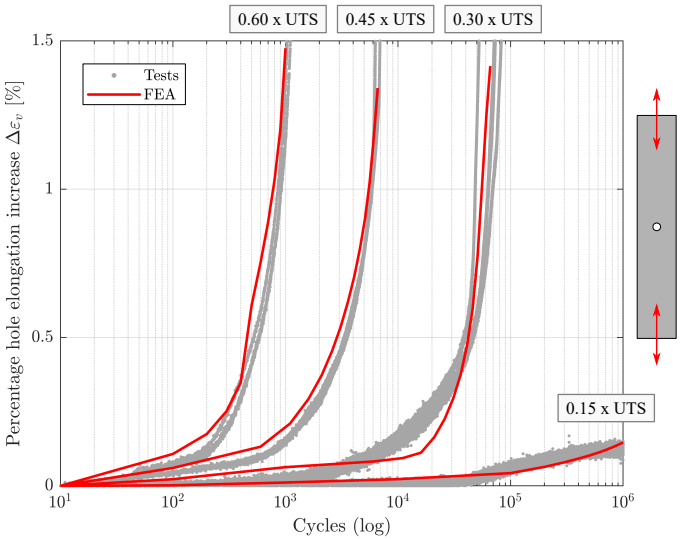

Figure 11: Percentage hole elongation increase in load-direction as predicted by the FML damage model for the cyclic FML open hole tension setup in comparison with respective experimental measurements.

between the vertical bolt and the counterbearing, as observed during testing. The buckling is induced during unloading as the inlays have been plastically deformed under tension during loading, thus yielding compressive stresses during unloading. This buckling effect is not captured by the FE-model, but is, however, unlikely to affect the fatigue results as no such buckling has been observed for the fatigue campaign, compare Fig. 14. The comparison of the predicted FRP damage in the topmost GFRP layer with a photograph of the tested specimen shows a sufficient similarity between simulation and experiment. The predicted "damage hot-spot" is located correctly in front of the vertical bolt. It is therefore assumed that the model of the T-bolt setup is generally valid, allowing to proceed with the fatigue analysis of the setup. Fig. 13 shows the result of the FML T-bolt fatigue simulation in comparison with the respective experimental measurements. Due to the cost- and time-intensive manufacturing process, only two specimens were tested under fatigue loading. To quantify the "global" state of damage, a damage parameter based on the applied machine force F and the resulting machinery displacement u is introduced, reading

$$D_{glob} = 1 - \frac{F(n)}{u(n)} \cdot \frac{u(10)}{F(10)} = 1 - \frac{E_{glob}(n)}{E_{glob}(10)}, \tag{24}$$

with n being the total number of cycles applied. As implied by Eq. 24, the damage D_{glob} is counted from the 10^{th} cycle onward, to account for settling effects during the first cycles. The comparison in Fig. 13 shows that the model accurately predicts the onset and progress of failure, represented by a sudden and steep increase of the global damage parameter D_{glob}. In addition to that, the level of damage prior to

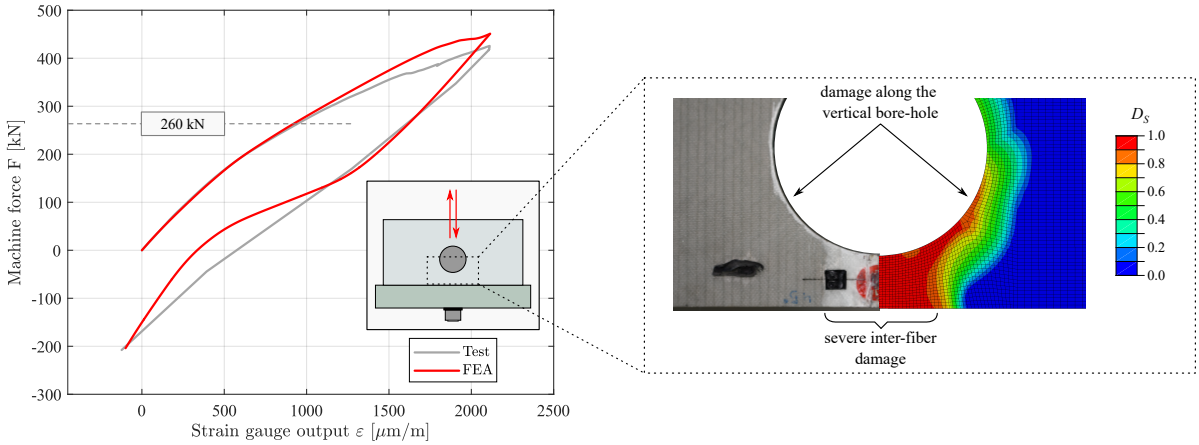

Figure 12: Simulation of a loading-unloading event of the FML T-bolt setup. The contour-plot to the right shows the distribution of maximum FRP damage in the topmost GFRP layer in comparison with an experimental photograph. No damage of the metallic inlays has been observed neither for the experimental test nor the FEA. The maximum load-level for the upcoming fatigue analysis of the setup is labeled.

final failure is predicted correctly by the model. To further increase the depth of validation for this setup, the specimens' damage modes are examined more in detail. As illustrated in Fig. 14 (left picture), the distribution of damage in the topmost FRP layer is matching the respective experimental photograph quite well, showing a vast spreading of inter-fiber failure right before and diagonal in front of the vertical bolt with respect to the load direction. To examine the failure mode of the inlays, the cyclically tested FML T-bolt specimens were incinerated. After incineration, the GFRP plies could be carefully removed. Fig. 14 (right picture) shows that the hot-spots of fatigue crack growth, as predicted by the inlay damage model, are in accordance with the experimentally observed crack pattern of a representative inlay. It is to note, that the fatigue tests were continued beyond the number of cycles being applied in the simulation (compare Fig. 13). This explains the topmost crack in the experiment being considerably longer than predicted by the model.

5. Conclusions

In this contribution, a novel FE-based fatigue damage modeling framework for FML bolted joints was presented and experimentally validated. While available FML assessment tools are mainly developed for FML with a high metal volume content (MVC), the presented framework was particularly designed for the fatigue analysis of FRP-based FML, featuring a minimal MVC. Accordingly, an explicit accounting for fatigue damage in the FRP plies was required. Furthermore, the framework should be able to predict

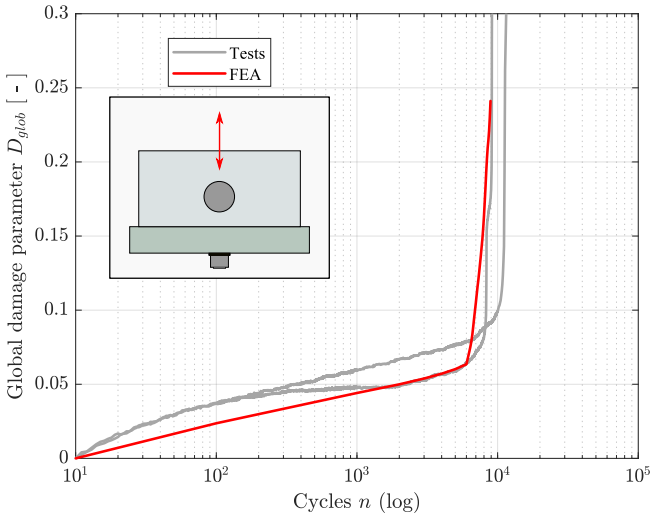

Figure 13: Comparison of global fatigue damage parameter D_{glob} evolution as predicted by the FML damage model and corresponding experimental measurements.

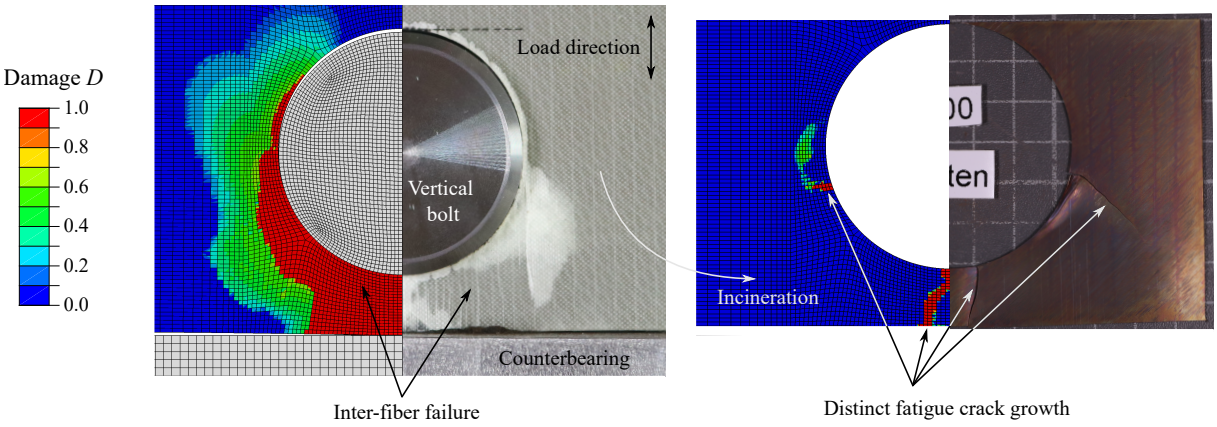

Figure 14: Comparison between the numerically predicted damage distributions and corresponding photographs taken from one of the cyclically tested FML T-bolt specimens after fatigue failure. The right comparison shows the fatigue crack pattern of a representative metallic inlay after incineration of a tested FML specimen and careful removal of the GFRP plies.

the bolted joint failure mode, while being applicable both in the low- and the high-cycle fatigue regime. This goal was successfully accomplished by combining two physically motivated material models, one for the metallic inlays and one FRP plies, implemented in one user-material (UMAT) subroutine for the commercial FE-software ABAQUS/Implicit.

In a first step, a novel continuum (fatigue) damage approach for the metallic inlays has been presented.

Using a cyclic elasto-plastic strain energy increment as primary fatigue metric, the inlay damage model is able to predict the initiation and growth of inlay fatigue cracks solely based on its physically motivated constitutive laws. As the approach accounts for the elasto-plastic material behavior of the inlays, these predictive abilities are available both in the low- and the high-cycle fatigue regime. Furthermore, the physical meaning of the fatigue metric supports a straight forward experimental calibration of the inlay damage model, as the metric is intrinsically valid for a wide range of stress-ratios.

To account for fatigue damage of the FRP plies, an energy-based continuum damage model, which was recently presented and validated by the authors in [11], has been adapted. Being based on a physically motivated energy hypothesis and the three-dimensional Puck fracture criteria, the damage model is able to closely capture the fatigue damage events of the FRP plies.

The results of the different validation campaigns demonstrated the predictive character and physical integrity of the static-cyclic FML damage modeling framework. While the results obtained by the FML open hole tension (OHT) campaign primarily proofed the applicability of the framework both in the low- and the high-cycle fatigue regime, the results of the T-bolt joint campaign were to demonstrate the ability of the framework to forecast the failure mode of a complex bolted joint setup. Here, especially the results obtained by the novel inlay damage model are noteworthy. Without any user-defined information concerning the laminate's failure mode (i.e. crack location and growth direction) given prior to or during the fatigue analysis, the model was able to correctly predict the multiple crack initiation and growth events in the metallic inlays of the FML T-bolt joint setup. It is thus to conclude, that the herein presented static-cyclic FML damage model holds a considerable predictive potential, which is yet unmatched by any available FML assessment tool. Due to the detailed and physically motivated representation of damage, the presented FML damage model is of particular interest for engineers dealing with the fatigue assessment of FRP-based FML bolted joints, as the presented framework is the first assessment tool specially developed for this use-case. Furthermore, as the model is implemented as a user-material (UMAT) subroutine for the commercial FE-software ABAQUS/CAE, the application of the damage model for complex analyses (like the presented T-bolt joint) is straight forward. Due to its proven validity, the presented FML damage model could be used in future as a benchmark tool to develop and verify new analytical or more simplified finite element approaches, which demand less computational costs and are thus highly appreciated by the industry.

In that context, further development should be considered to improve the model's efficiency in terms of required wall-clock time per analysis. Currently, the fatigue analysis of a complex model like the T-bolt setup might take up to several days until accomplishment. To increase the efficiency of the model, while preserving its accuracy, an adaptive cycle jump technique should be implemented.

Concerning the results presented in Fig. 9, the inlay fatigue initiation criterion should be further examined. Although the inlay fatigue damage model performed well within the FML analyses (compare Fig. 11 and 13), the validity of the ΔW^{tot} formulation used in this study should be investigated also for stress ratios including compression, i.e. $R < 0$ and $R > 1$. Respective tests were not performed for the current study, as considerable experimental effort is required to test the inlay sheet metal (0.25 mm thickness) under compressive loading.

Acknowledgments

The work presented in this paper was funded by the Federal Ministry of Education and Research of the Federal Republic of Germany under the project LENAH - Hybrid laminates and nanoparticle reinforced materials for improved rotor blade structures (grant number 03SF0529A) and by the Federal Ministry of Economics and Energy under the project HANNAH - Challenges of the industrial application of nanomodified and hybrid material systems in lightweight rotor blade construction (grant number 0324345A). Special thanks go to Markus Mlinaric, who contributed to the success of this work by conducting the water-jet cutting of the stainless steel and FML open hole tension specimens used for the experimental campaigns in this study.

References

[1] A. Ataş, C. Soutis, Damage and failure analysis of bolted joints in composite laminates, in: The Structural Integrity of Carbon Fiber Composites, Springer International Publishing, 2016, pp. 591–644. doi:https://doi.org/10.1007/978-3-319-46120-5_21.

[2] A. Fink, P. Camanho, J. Andrés, E. Pfeiffer, A. Obst, Hybrid CFRP/titanium bolted joints: Performance assessment and application to a spacecraft payload adaptor, Composites Science and Technology 70 (2) (2010) 305–317. doi:10.1016/j.compscitech.2009.11.002.

[3] C. Gerendt, A. Dean, T. Mahrholz, R. Rolfes, On the progressive failure simulation and experimental validation of fiber metal laminate bolted joints, Composite Structures 229 (2019) 111368. doi:10.1016/j.compstruct.2019.111368.

[4] J. Lopes, L. Reis, D. Stefaniak, M. Freitas, P. Camanho, Mechanical characterisation of CFRP-steel hybrid composites, International Journal of Automotive Composites 2 (2) (2016) 139. doi:10.1504/ijautoc.2016.082071.

[5] J. J. Homan, R. P. G. Müller, F. Pellenkoft, J. J. M. de Rijck, Fatigue of riveted joints, Springer Netherlands, 2001.

[6] W. Wang, C. Rans, R. Benedictus, Theoretical analysis of fatigue failure in mechanically fastened fibre metal laminate joints containing multiple cracks, Engineering Failure Analysis 91 (2018) 151–164. doi:10.1016/j.engfailanal.2018.03.012.

[7] F. Ellyin, Fatigue Damage, Crack Growth and Life Prediction, Springer Netherlands, 1996. doi:10.1007/978-94-009-1509-1.

[8] R. Alderliesten, How proper similitude can improve our understanding of crack closure and plasticity in fatigue, International Journal of Fatigue 82 (2016) 263–273. doi:10.1016/j.ijfatigue.2015.04.011.

[9] H. Yu, D. Y. Jeong, Impact dynamics and puncture failure of pressurized tank cars with fluid–structure interaction: A multiphase modeling approach, International Journal of Impact Engineering 90 (2016) 12–25. doi:10.1016/j.ijimpeng.2015.11.014.

[10] M. Á. Caminero, F. J. Montáns, An enhanced algorithm for nested surfaces plasticity using the implicit mróz translation rule, Computers & Structures 84 (26-27) (2006) 1684–1695. doi:10.1016/j.compstruc.2006.04.001.

[11] C. Gerendt, A. Dean, T. Mahrholz, N. Englisch, S. Krause, R. Rolfes, On the progressive fatigue failure of mechanical composite joints: Numerical simulation and experimental validation, Composite Structures 248 (2020) 112488. doi:10.1016/j.compstruct.2020.112488.

[12] D. Pfanner, Zur Degradation von Stahlbetonbauteilen unter Ermüdungsbeanspruchung, Ph.D. thesis, Institut für Stahlbeton- und Spannbetonbau, Ruhr-Universität Bochum (2003).

[13] ABAQUS/Standard User's Manual, Version 2019, Dassault Systèmes Simulia Corp, United States, 2019.

[14] T. London, D. D. Bono, X. Sun, An evaluation of the low cycle fatigue analysis procedure in abaqus for crack propagation: Numerical benchmarks and experimental validation, 2015.

[15] F. Meier, C. Schwarz, E. Werner, Numerical calculation of the tangent stiffness matrix in materials modeling, PAMM 14 (1) (2014) 425–426. doi:10.1002/pamm.201410200.

[16] M. Knops, Analysis of Failure in Fiber Polymer Laminates, Springer Berlin Heidelberg, 2008. doi:10.1007/978-3-540-75765-8.

[17] V. Martínez, A. Güemes, D. Trias, N. Blanco, Numerical and experimental analysis of stresses and failure in t-bolt joints, Composite Structures 93 (10) (2011) 2636–2645. doi:10.1016/j.compstruct.2011.04.031.

[18] M. R. Hirsch, Fretting behavior of aisi301 stainless steel sheet in full hard condition, Master's thesis, Georgia Institute of Technology (2008).